



Full length article



## Local structure modification around Si atoms in Si-implanted monocrystalline $\beta$ -Ga<sub>2</sub>O<sub>3</sub> (100) under heated substrate conditions

I.N. Demchenko<sup>a,\*</sup>, Y. Syryanyy<sup>a,b</sup>, A. Shokri<sup>a</sup>, Y. Melikhov<sup>c</sup>, J. Domagała<sup>d</sup>, R. Minikayev<sup>d</sup>, A. Derkachova<sup>d</sup>, F. Munnik<sup>e</sup>, U. Kentsch<sup>e</sup>, M. Zajac<sup>f</sup>, A. Reck<sup>g</sup>, N. Haufe<sup>g</sup>, Z. Galazka<sup>h</sup>

<sup>a</sup> Institute of Plasma Physics and Laser Microfusion, ul. Hery 23, Warsaw, 01-497, Poland

<sup>b</sup> Institute of Microelectronics and Optoelectronics, Warsaw University of Technology, Koszykowa 75, Warsaw, 00-662, Poland

<sup>c</sup> Institute of Fundamental Technological Research Polish Academy of Sciences, ul. Pawlowskiego 5b, Warsaw, 02-106, Poland

<sup>d</sup> Institute of Physics PAS, al. Lotników 32/46, Warsaw, 02-668, Poland

<sup>e</sup> Helmholtz-Zentrum Dresden-Rossendorf, Bautzner Landstraße 400, Dresden, 01328, Germany

<sup>f</sup> National Synchrotron Radiation Centre SOLARIS, Jagiellonian University, Czerwone Maki 98, Kraków, 30-392, Poland

<sup>g</sup> Fraunhofer Institute for Photonic Microsystems (IPMS), Center Nanoelectronic Technologies, An der Bartlake 5, Dresden, 01109, Germany

<sup>h</sup> Leibniz-Institut für Kristallzüchtung, Max-Born-Straße 2 12489, Berlin, Germany

### ARTICLE INFO

#### Keywords:

$\beta$ -Ga<sub>2</sub>O<sub>3</sub>

WBG

Implantation

XRD

RBS/PIXE/c

XANES

TEM

DFT

FMS

### ABSTRACT

Doping of  $\beta$ -Ga<sub>2</sub>O<sub>3</sub> (100) with Si by ion implantation onto heated substrates is investigated. The study reveals complex ion beam-induced defect processes in  $\beta$ -Ga<sub>2</sub>O<sub>3</sub>, characterized by the formation of various defect types and their temperature-dependent transformation. By employing X-Ray Diffraction, Rutherford Backscattering Spectrometry, Particle-Induced X-Ray Emission, X-ray Absorption Near Edge Structure Spectroscopy, Transmission Electron Microscopy, and Density Functional Theory analyses, we examine lattice deformation, identify the local environment of dopants, assess electronic structure modifications, and verify the presence of extended defects induced by ion implantation. Our findings highlight the predominant contribution of substitutional and interstitial Si ions incorporated into complexes that act as donors manifesting n-type conductivity, while some fraction of the defects form complexes that act as traps for charge carriers. Notably, no monoclinic phase transformations were observed during implantation despite substrate temperature variations from 300 to 800 °C.

### 1. Introduction

While silicon-based power devices currently dominate the market, they are approaching fundamental performance limitations preventing commercial power systems from becoming smaller and more efficient. Wide bandgap (WBG) materials, such as GaN and SiC, are now considered the next-generation materials for power electronics. A new class of power devices based on ultra-WBG semiconductors, including AlN,  $\beta$ -Ga<sub>2</sub>O<sub>3</sub>, and diamond, can potentially revolutionize the power electronics industry. Particular scientific and technological attention is paid to monoclinic  $\beta$ -Ga<sub>2</sub>O<sub>3</sub>, which is the most stable polymorph, that can be grown directly from the melt, including the Edge-Defined Film-Fed Growth [1], the Czochralski [2], and Bridgman [3] methods, enabling large wafers up to 6 inches in diameter [4].  $\beta$ -Ga<sub>2</sub>O<sub>3</sub> has a bandgap of 4.85 eV [5], offers a wide range of free electron concentrations of  $\sim 10^{14}$

$\sim 10^{20} \text{ cm}^{-3}$  and relatively high electron mobility approaching  $190 \text{ cm}^2 \text{ V}^{-1} \text{ s}^{-1}$  [6–8]. Further, it has a high breakdown electric field of 8 MV/cm (theoretical) to handle high voltages and a large Baliga Figure of Merit to reduce switching losses [9]. More details on crystal and film growth, device fabrication, and physical properties of Ga<sub>2</sub>O<sub>3</sub> can be found elsewhere [10,11]. Recent notable achievements include the integration of ion implantation to engineer a Ga<sub>2</sub>O<sub>3</sub> transistor [12], a technique extensively employed in the mass production of commercial semiconductor devices. Ion implantation aims to either decrease ohmic contact resistance (shallow donors) and/or to realize potential barriers for voltage blocking (compensating acceptors). Shallow donors applied by ion implantation into  $\beta$ -Ga<sub>2</sub>O<sub>3</sub> include Si, Sn, and Ge [12–16], while compensating acceptors cover Mg and N [12–17]. Ion implantation has been demonstrated mainly on commercially available substrates/films with (010), (001), and ( $\bar{2}01$ ) surface orientations, with little work done

\* Corresponding author.

E-mail address: [iraida.demchenko@ifilm.pl](mailto:iraida.demchenko@ifilm.pl) (I.N. Demchenko).

<https://doi.org/10.1016/j.actamat.2025.121036>

Received 29 October 2024; Received in revised form 16 March 2025; Accepted 9 April 2025

Available online 11 April 2025

1359-6454/© 2025 The Authors. Published by Elsevier Inc. on behalf of Acta Materialia Inc. This is an open access article under the CC BY license (<http://creativecommons.org/licenses/by/4.0/>).

on the (100) orientation, which is the easiest cleavage plane, has the lowest formation energy, and offers a great smoothness, what is, in particular, important for  $\delta$ -doping. Further, extensive development of homoepitaxial film growth on the (100) surface with a dedicated offcut ( $2\text{--}6^\circ$  toward  $[00\bar{1}]$ ) resulted in great electrical properties [18,19] and power device fabrication with high performance [20,21]. Due to differences in surface properties and anisotropy, all process steps in a device fabrication chain must be studied and developed separately. For instance, structural defects that are mostly aligned with the  $[010]$  direction will have a different impact on thick film growth and device operation (leakage current) depending on the surface orientation. It has also been shown that ohmic contact resistance strongly depends on the surface orientation [22]. Therefore, we address in the present report Si ion implantation into (100) oriented wafers of  $\beta\text{-Ga}_2\text{O}_3$  grown by the Czochralski method [2] to reveal defect formation that may impact electronic device operation.

However, ion implantation into (100)-oriented substrates presents challenges. These atomic planes are densely packed and are more susceptible to damage. Post-implantation annealing or heating during implantation may be less effective in repairing damage and activating dopants due to the higher defect concentration for  $\beta\text{-Ga}_2\text{O}_3$  (100) substrates. This can subsequently impact the electrical activation of implanted dopants and overall device performance. Ion implantation into heated  $\beta\text{-Ga}_2\text{O}_3$  substrates introduces further complexity due to the potential for reorganization and/or creation of additional complexes around the implanted ions during implantation. Among the studies on (100)-oriented  $\beta\text{-Ga}_2\text{O}_3$ , to the best of our knowledge, only three have focused on ion implantation at room and elevated temperatures using Ge [16], N [18], and Eu [61]. Tetzner et al. [16] studied  $\text{Ge}^{4+}$  implantation in MOVPE-grown  $\beta\text{-Ga}_2\text{O}_3$  films on (100)-oriented native wafers, followed by annealing at  $900\text{--}1200^\circ\text{C}$ . Their findings indicate that surface morphology remains stable up to  $1100^\circ\text{C}$  but changes at  $1200^\circ\text{C}$ . The resistivity decreases with annealing, reaching a minimum at  $1100^\circ\text{C}$ , while SIMS profiles reveal Ge penetration up to 250 nm with minimal diffusion upon annealing. In another study, Tetzner et al. [18] investigated  $\text{N}^+$  implantation under energies of  $30\text{--}360$  keV and doses of  $8 \times 10^{12}\text{--}3 \times 10^{13}$   $\text{cm}^{-2}$ . The post-implantation sheet resistance increased by nine orders of magnitude and remained stable up to  $600^\circ\text{C}$  but decreased at  $800^\circ\text{C}$ , likely due to electron trapping at implantation-induced defects. Structural analysis revealed extended defects, which recovered after annealing, though point defects persisted, acting as charge traps. A study of Eu implantation into  $\beta\text{-Ga}_2\text{O}_3$  (100) single crystals grown via the floating zone technique was performed by Peres et al. [61]. It was concluded that the implantation at intermediate temperatures ( $\sim 600^\circ\text{C}$ ) reduced damage and promoted Eu substitution in the Ga lattice, enhancing optical activation. However, defect accumulation was complex, with implantation damage initially decreasing at  $400\text{--}600^\circ\text{C}$  but increasing again at higher temperatures due to defect clustering. Analysis of Eu  $L_3$ -edge XANES spectra revealed a strong dependence of  $\text{Eu}^{3+}/\text{Eu}^{2+}$  ratios on implantation and annealing conditions, with charge state stabilization influenced by defect interactions rather than a direct correlation with substitutional fraction. In contrast to the aforementioned studies, the present study focuses specifically on the modification of the local structural environment of the implanted ion (Si in our case), including intrinsic point defects in the  $\beta\text{-Ga}_2\text{O}_3$  (100) host matrix under heated substrate conditions. This aspect has been largely unexplored in prior research. Therefore, it is important to have a deeper understanding of the lattice location of dopants and the role of native defects (such as oxygen/gallium vacancies/interstitials) in residual conductivity relative to extrinsic impurities. This knowledge is essential as it should enable the fabrication of devices based on a manufacturable all-ion-implanted process like for MOSFETs. Moreover, the acquired knowledge could lead to more efficient electronic devices capable of operating under harsh conditions. Notably, the current state of  $\beta\text{-Ga}_2\text{O}_3$  (100)-based materials lacks reports dedicated to structural

studies of materials modified by light-ions implantation, which this paper aims to address.

## 2. Experimental details

### 2.1. Crystal samples; Rutherford backscattering spectrometry, particle-induced X-Ray emission (RBS/PIXE)

Crystal samples selected for the present study were prepared from a 2-inch diameter bulk  $\beta\text{-Ga}_2\text{O}_3$  single crystal grown along the  $[010]$  crystallographic direction using the Czochralski method at Leibniz-Institut für Kristallzüchtung (Berlin, Germany). The crystal was grown from an Ir crucible with an oxygen concentration of 8 vol. % in the growth atmosphere with no intentional dopants (for further details, see [2,23]). The samples of size  $5 \times 5 \times 0.5$   $\text{mm}^3$  were (100) oriented and a double-side chemical-mechanical polishing was performed. The samples were semiconducting with the free electron concentration and electron mobility (from Hall effect measurements) of  $3.4 \times 10^{17}$   $\text{cm}^{-3}$  and  $118$   $\text{cm}^2\text{V}^{-1}\text{s}^{-1}$ , respectively. To select optimal implantation parameters that would prevent mechanical degradation of the gallium oxide crystal surface, the samples were implanted under a heated substrate condition while maintaining a constant fluence of  $5 \times 10^{15}$   $\text{at}/\text{cm}^2$  (with a flux  $1.72 \times 10^{11}$   $\text{s}^{-1}\text{cm}^{-2}$ ) at an energy of 175 keV. The implantation angle was about  $7^\circ$  to avoid channeling. The substrate temperature was kept constant throughout each implantation process, with selected temperatures ranging from  $300$  to  $800^\circ\text{C}$ . The minimum temperature of  $300^\circ\text{C}$  was selected because at room temperature the samples degraded during implantation and the maximum temperature of  $800^\circ\text{C}$  was selected because at  $900^\circ\text{C}$  the crystal was contaminated by the clamps. To monitor the lattice disorder and the Si lattice site location with depth resolution, RBS/c measurements were carried out using a 1.7 MeV  $\text{He}^+$  beam and a Si pin diode as a detector placed at a backscattering angle of  $170^\circ$ . Random and aligned spectra along the  $[201]$  direction were acquired to determine minimum yield functions. Moreover, PIXE/c experiments were carried out on samples using a Silicon Drift Detector with an area of  $80$   $\text{mm}^2$ .

### 2.2. X-ray diffraction (XRD)

High-resolution (HR) XRD was performed on a PANalytical X'Pert Pro MRD XL diffractometer (delivering  $\text{Cu K}_{\alpha 1}$  radiation,  $\lambda=1.54056$   $\text{\AA}$ ) equipped with a fourfold (220) Ge monochromator and threefold (022) Ge analyzer.

### 2.3. X-ray absorption near edge structure (XANES) spectroscopy

The X-ray absorption experiments were performed at the Solaris synchrotron on the PIRX beamline. The XANES spectra were obtained recording the total electron yield (TEY) and total fluorescence yield (TFY or FLUO) signals from the samples while scanning the photon energy over the Si K edge region. The X-ray absorption experiments were carried out with the polarization vector of the synchrotron radiation oriented close to the “magic” angle, i.e. the angle at which the absorption cross-section becomes independent of the orbital orientation. After normalization to the photon flux, the recorded XANES spectra were subjected to subtraction of a linear background, which was fitted to the flat pre-absorption-edge region. For quantitative comparison, the spectra were then normalized to the atomic limit, the range of about 100 eV photon energy above the absorption edge, where no angular dependence is observed. To interpret the experimental XANES signal, a broad spectrum of intrinsic/extrinsic point defects and their complexes was theoretically analyzed using a Green's function methodology implemented within the software package FEFF [24].

## 2.4. Transmission electron microscopy (TEM)

TEM studies were conducted on a Tecnai F20 (twin lens configuration) model from the company FEI at 200 kV acceleration voltage (field emission gun). For the analyses, electron-transparent lamellae (prepared by the Focused Ion Beam (FIB) technique) were examined under Brightfield and scanning transmission electron microscopy (STEM) conditions with different beam diameters (spot sizes) and, thus, different current doses on samples, as well as varying condenser/objective apertures. In addition, selected area diffraction (SAD) experiments were carried out at lower magnifications (size limitations for high resolution). The analysis was conducted along the [010] direction. Fast Fourier transform (FFT) simulations complemented the investigations at higher resolutions to clear up possible second-phase influences in the Si-implanted  $\beta$ -Ga<sub>2</sub>O<sub>3</sub> under heated substrate conditions. The evaluation of the images was done using the Gatan Digital Micrograph (GMS 3) software.

## 2.5. Computational methods

### 2.5.1. Hybrid-density functional theory (H-DFT)

Using Vienna Ab-initio Simulation Package (VASP, v. 6.3.2) and applying projector augmented wave potentials, we performed first-principles density functional theory (DFT) calculations [25–27, 28] to study the monoclinic phase of  $\beta$ -Ga<sub>2</sub>O<sub>3</sub> structure with the space group of C2/m which includes 20 atoms in its conventional unit cell. An energy cutoff of 510 eV, convergence tolerance of <0.03 eV/Å, and energy tolerance of <0.0001 eV with a  $2 \times 2 \times 2$  k-point grid were used for optimization calculations of 160-atom of  $1 \times 4 \times 2$  supercells with the symmetry turned off. Spin-polarized HSE06 hybrid functional [29] was utilized with a fixed screening parameter and a 32 % mixing parameter in order to get accurate structural and electronic properties. Our relaxation calculations resulted in  $a = 12.221$  Å,  $b = 3.028$  Å and  $c = 5.872$  Å for lattice constants for the unit cell of  $\beta$ -Ga<sub>2</sub>O<sub>3</sub> and the band gap of the pristine structure is  $E_g = 4.73$  eV.

The formation energy ( $E_q^f$ ) of an impurity with a charge state of  $q$  is computed as [30]:

$$E_q^f = E_{tot}(X_q) - E_{tot}(bulk) - \sum_i n_i \cdot \mu_i + q \cdot (E_{VBM} + E_F) + E_{corr}, \quad (1)$$

where  $E_{tot}(X_q)$  is the total energy of the supercell with the defect in the charge state  $q$ ,  $E_{tot}(bulk)$  is the total energy of the defect-free structure. The term  $n_i \cdot \mu_i$  accounts for the change in the number of atoms  $n_i$  of type  $i$  with a chemical potential  $\mu_i$  due to the defect formation, with  $n_i$  being positive or negative depending on whether an atom is removed or added, respectively. For this study, the following chemical potentials  $\mu_i$  of the elements were selected:  $\mu_{Si} = -5.69$  eV (calculated from Si bulk),  $\mu_{Ga} = -3.38$  eV (calculated from bulk Ga metal for Ga-rich) and  $\mu_O = -7.187$  eV (calculated from O<sub>2</sub> molecules for Ga-poor). The term  $q \cdot (E_{VBM} + E_F)$  describes the change of the formation energy in case  $q$  electrons are removed or added, where  $E_F$  represents the Fermi energy of  $\beta$ -Ga<sub>2</sub>O<sub>3</sub> and  $E_{VBM}$  is the energy of valence band maximum. The Freysoldt-Neugebauer-Van de Walle (FNV) correction term,  $E_{corr}$ , is applied to eliminate spurious electrostatic interactions between defects and their images [31]. A value of 10 is used for the experimental dielectric constant of the  $\beta$ -Ga<sub>2</sub>O<sub>3</sub> matrix [32] to compute  $E_{corr}$ .

Using Eq. (1), a thermodynamic transition level can be also identified [33]:

$$\epsilon(q_1 / q_2) = \frac{E_{q_1}^f|_{E_F=0} - E_{q_2}^f|_{E_F=0}}{q_2 - q_1}, \quad (2)$$

where  $E_q^f|_{E_F=0}$  is the formation energy of the defect in charge state  $q$  when the Fermi energy  $E_F$  is set to zero.

### 2.5.2. Full multiple scattering (FMS)

XANES spectra were calculated using the *ab initio* code FEFF8 within the real-space full multiple-scattering (FMS) approach [34,35]. This code implements the single-electron theory, based on a self-consistent real-space Green's function formalism and final-state potentials considering an appropriately screened core hole. For a better understanding, the interpretation of the experimental XANES spectra was performed in terms of real space multiple scattering formalism [36]. The FMS calculations of the silicon K-edge XANES were performed for different cluster sizes (specified as spheres of a given radius around the absorbing atom) of the corresponding model, which has the monoclinic structure (with space group C2/m and the lattice parameters  $a = 12.2140$  Å,  $b = 3.0371$  Å,  $c = 5.7981$  Å). The best results were obtained using the Hedin-Lundqvist self-energy together with an additional energy shift (set in the EXCHANGE card) to set the Fermi level. Self-consistency was achieved for a cluster size of about 4.7 Å (the SCF card) corresponding to 45 atoms, including the absorber. In the final analysis, the FMS was used (the FMS card) for a cluster of radius 7.5 Å surrounding the absorber. Lorentzian broadening with HWHH (half-width at half-height) equal to 0.1 eV was used for the calculated spectra. All muffin-tin spheres were automatically overlapped by 15 % (the AFOLP card) to reduce the effect of potential discontinuities at the muffin tins. XANES spectra were calculated in the presence of an appropriately screened core-hole according to the final state rule.

## 3. Results and discussion

The investigations of ion-implanted layers, particularly for implantation at elevated temperatures, which is often used during device manufacturing, are important for understanding the evolution of structural changes in dependence on implantation temperature. Fig. 1(a) shows the RBS spectra of the virgin  $\beta$ -Ga<sub>2</sub>O<sub>3</sub> and the samples implanted by Si at different substrate temperatures,  $T_S$ , varying from 300 to 800 °C. The calculated average concentration of silicon for 300 nm depth of  $\beta$ -Ga<sub>2</sub>O<sub>3</sub> is equal to 0.20 at %. The defect profiles, corresponding to the relative number of displaced Ga atoms, were determined by calculating the difference between the minimum yield of the samples implanted by Si and the pristine samples as a function of depth, and subsequently subtracting the dechanneling yield. The rate of the dechanneling of beam particles at defects was estimated using the DICADA2 code for compound crystals [37]. This code relies on the discontinuous dechanneling model and assumes randomly displaced atoms as the origin of increased backscattering yield in first order. The depth range of the defect profiles is limited by the onset of the O-signal in the RBS spectrum. Given profiles are presented in Figure 1(b). The Si (violet line) and Ga&O vacancy (brown line) profiles, calculated using the TRIM/SRIM program [38], are also shown for comparison. The defect distribution profile of silicon calculated using TRIM/SRIM at room temperature (RT) is located closer to the surface than the maxima of the relative defect concentration profiles for the implanted samples. Detection of Si in  $\beta$ -Ga<sub>2</sub>O<sub>3</sub> using RBS is challenging due to the low scattering cross-section of a low-Z impurity (Si) and the continuous background arising from overlap with ions scattered from the heavier  $\beta$ -Ga<sub>2</sub>O<sub>3</sub> monocrystal. In the case of  $\beta$ -Ga<sub>2</sub>O<sub>3</sub>:Si, the maxima of 'relative defect concentration' (RDC) are increasingly shifted away from the sample surface with rising  $T_S$ . RDC intensity (including visible tails) progressively decreases with increasing  $T_S$ . The behavior of the RDC curves presented in Figure 1(b) for  $T_S$  above 300 °C, namely, the shift of the RDC maximum to greater depths compared to SRIM predictions, closely resembles the trend reported by Peres et al. [61]. In their study, Eu was implanted into similarly oriented gallium oxide monocrystal at a fluence of  $1 \times 10^{15}$  at/cm<sup>2</sup> over a temperature range of 20–1000 °C. Their findings suggest that defect migration occurs during implantation, leading to accumulation near the interface between the implanted and pristine regions of the sample. Our results indicate that diffusion associated with the implantation temperature (and probably implantation time) plays a dominant

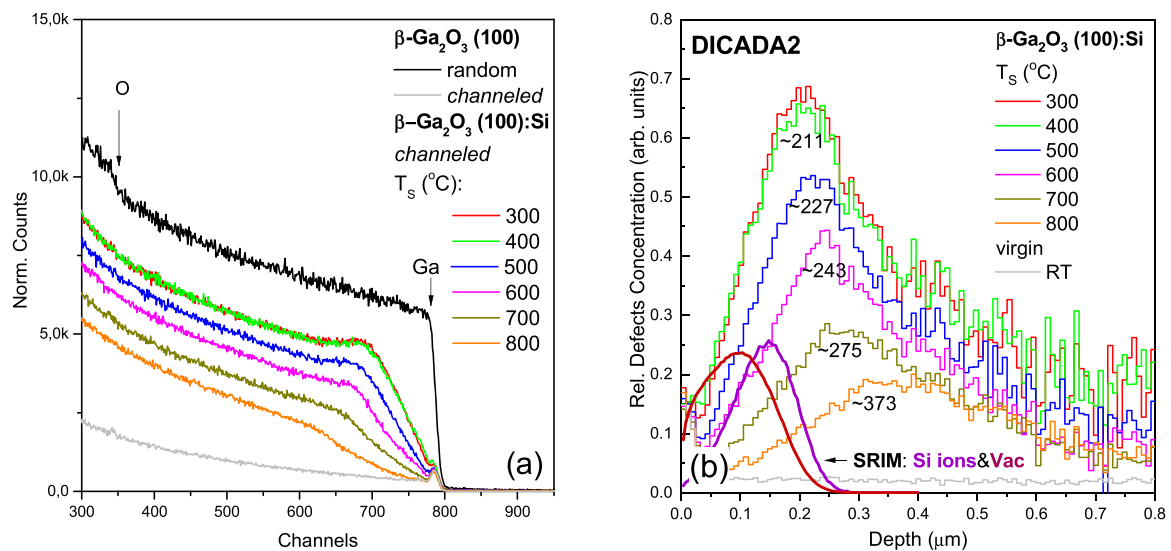


**Fig. 1.** (a) RBS random and [201] aligned (channeled) spectra for the  $\beta\text{-Ga}_2\text{O}_3$  monocrystals implanted by Si at different substrate temperature ( $T_s$ ) implantation conditions. (b) Relative defect concentration as a function of depth extracted using the DICADA2 program from the RBS spectra in (a). For comparison, the Si (thick violet line) and Ga/O vacancy (thick brown line) profiles calculated using the TRIM/SRIM program [38] are also shown in (b) (not to scale). The numbers near the relative defect concentration distribution lines correspond to the depth positions of the maxima (in nm).

role. This is evidenced by the gradual decrease in defect concentration and the progressive shift of the RDC maxima deeper into the sample with increasing  $T_s$ .

Since the contribution of direct backscattering and dechanneling to the aligned RBS spectra depends on the type of defects, the RDC behavior shown in Figure 1(b) indicates a significant decrease in both point and extended defects concentration. It is well-recognized that point defects are characterized by uncorrelated displaced lattice atoms. In this case, the contribution of direct backscattering is significant and represented by maxima visible in Figure 1(b). Conversely, in the case of extended defects, a correlated displacement of lattice atoms occurs, and the contribution of direct backscattering is negligible. This means that the channeled RBS spectra are mainly determined by the dechanneling of the  $\text{He}^+$  ions that are used for RBS. This effect is illustrated in Figure 1(b) by the above-mentioned visible tails. The elevation of the tail of the relative defect concentration distribution is a representation of extended defects present in all samples. This behavior coincides well with the results presented in [62] (there, see Fig. 5 and the corresponding discussion) for silicon and confirms the dependence we presented in Figure 1(b). Note that according to [62], the first version of the DICADA code had an option to consider extended defects for single-element crystals (e.g., Si). Consequently, according to the results obtained, the number of extended defects decreased with increasing  $T_s$ . Although the DICADA2 code is not capable of simulating extended defects, the identification of their specific type is best achieved using TEM. This approach is considered optimal by the authors, given the ambiguity of existing theoretical approximations. Our conclusions are supported by the subsequent results from the TEM study (data are not presented here), for which lamellae were analyzed at different sample depths. The study of these lamellae confirmed our assumptions derived from the qualitative analysis of the RBS and HR XDR data. Namely, the depth analysis of the samples indicated the presence of extended defects (dislocations and stacking-faults) at depths of 200 nm and 350 nm for samples with lower  $T_s$ . These depths are deeper than 180 nm, i.e. the depth level of the peak silicon distribution predicted by SRIM calculations at room temperature. At higher implantation temperatures, the number of extended defects significantly decreases. A defect-free gallium oxide structure is observed at a depth of 800 nm.

The normalized yield for the RBS,  $\chi_{\text{Ga}}$  or the PIXE Si X-ray signals,  $\chi_{\text{Si}}$ , are defined as the ratio of the channeled yield to the corresponding

random yield. The fraction of nonrandom Si,  $f_{\text{nr}}$ , can then be calculated by comparing  $\chi_{\text{Ga}}$  and  $\chi_{\text{Si}}$  from the  $\beta\text{-Ga}_2\text{O}_3\text{:Si}$  sample using a well-known equation  $f_{\text{nr}} = (1 - \chi_{\text{Si}})/(1 - \chi_{\text{Ga}})$  [39]. The resultant  $f_{\text{nr}}$  for the studied samples obtained from the [201] channeled projection is shown in Figure S1. For Si implanted in  $\beta\text{-Ga}_2\text{O}_3$  in the  $T_s$  range of 300–600 °C, the  $f_{\text{nr}}$  values are quite similar, exhibiting a visible downward trend. However, as  $T_s$  during the implantation process increases to 700–800 °C, the  $f_{\text{nr}}$  values decrease. The observed behavior, at this point, can be explained if some Si atoms are ‘visible’ in the channeling direction and the X-ray emission coming from these interstitial or displaced  $\text{Si}_{\text{Ga}}$  atoms [39]. Therefore,  $f_{\text{nr}}$  calculated from  $\chi_{\text{Si}}$  does not represent the true nonrandom Si fraction. Indeed, the Relative Disorder Fraction ( $\chi/\chi_{\text{random}}$ ) from the RBS/c measurements for the samples with the  $T_s$  of 700–800 °C and for the virgin crystal falls in the range  $0.1 \leq \chi/\chi_{\text{random}} \leq 0.5$ . This region is associated with low to moderate disorder. On the other hand, the samples with lower  $T_s$  have  $\chi/\chi_{\text{random}} \geq 0.5$ , which is associated with a severe disorder. The equation for  $f_{\text{nr}}$  works best in single-crystal materials with low-to-moderate disorder under precisely controlled channeling conditions. In the cases where disorder is too high, defects cluster, or the beam is misaligned, the extracted  $f_{\text{nr}}$  may not accurately reflect the actual defect fraction, which agrees well with the results we obtained. Nevertheless, the overall decrease in  $f_{\text{nr}}$  for the [201] channeling direction with an increase in  $T_s$  indicates that the heating process during implantation may promote Si random precipitation or formation of complexes. These results are supported by the results of PIXE/RBS/c presented in Fig. 2 which will be discussed further. Although it is not possible to identify the form of these random precipitates/complexes from the present study, earlier reports on annealing of  $\beta\text{-Ga}_2\text{O}_3\text{:Si}$  suggest that Si removed from the lattice sites forms  $\text{SiO}_2$  inclusions when the annealing takes place at 1100 °C [40]. Additionally, several reports on similar systems using scanning transmission electron microscopy and positron annihilation spectroscopy techniques have indicated the formation of complexes consisting of cation interstitial atom bound by two gallium vacancies [41–43].

Let us continue the discussion of the results obtained from the  $\beta\text{-Ga}_2\text{O}_3\text{:Si}$  samples implanted in a heated substrate, at temperatures ranging from 300 to 800 °C, by estimating the expected structural changes. XRD is widely used to investigate structure changes during semiconductor processing as a routine method for fast and reliable diagnostics [44]. In particular, HR XRD is used to estimate structural

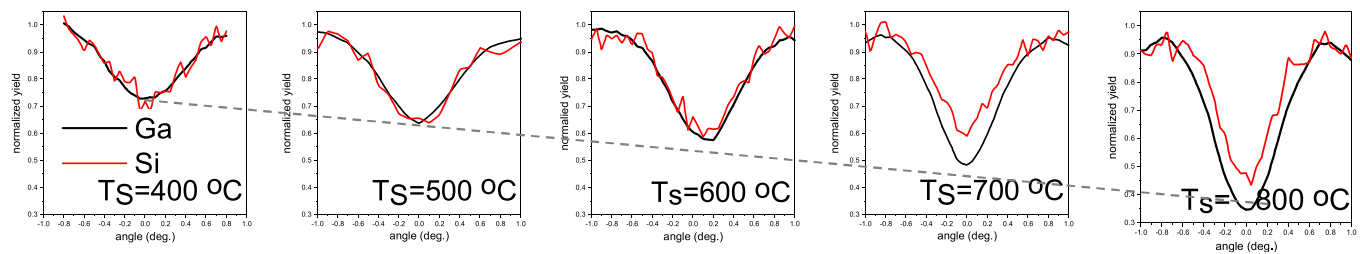


Fig. 2. PIXE/RBS/c angular distributions of channeling in the [201] direction for the  $\beta$ -Ga<sub>2</sub>O<sub>3</sub>:Si samples implanted under different substrate temperatures,  $T_s$ .

changes after ion implantation [45] and subsequent annealing [46]. In many cases, XRD characterization is limited by quick analysis of strain and layer thickness values using oscillation positions [40]. However, careful XRD investigation, including numerical simulations, allows us to obtain the depth distribution of strain and damage with depth [47]. The  $2\theta/\omega$  scans across the 400 symmetric reflection are shown in Fig. 3(a). The black line corresponds to the pristine sample with a so-called substrate peak at  $2\theta \approx 30.075^\circ$ , marked as 'v', which comes from the  $\beta$ -Ga<sub>2</sub>O<sub>3</sub> monocrystal. In addition, intense fringes are visible with the maximum deviation labeled as '1' ( $2\theta \approx 29.88^\circ$ ), '2' ( $2\theta \approx 29.92^\circ$ ) and '3' ( $2\theta \approx 29.99^\circ$ ) for samples implanted in the heated substrate at  $T_s$  of 300, 500 and 700 °C, respectively. For the sample implanted at  $T_s = 800$  °C (magenta line, '4'), the  $\beta$ -Ga<sub>2</sub>O<sub>3</sub> matrix relaxes, and only a small strain remains in the layer. The origin of the oscillation fringes observed on the left side of the basal (400) reflection peak from the substrate is associated with damage and strain introduced by ion implantation near the surface. The implantation process forms a layer with a disrupted crystal lattice, where there is a gradual transition from a more deformed structure to the undisturbed bulk crystal. The resulting strain gradient leads to lattice expansion, giving rise to asymmetric diffraction streaks in the HRXRD pattern. This phenomenon is extensively described in the literature, for instance, in [64,65]. The lattice expansion, increasing (100) interplanar spacing, could presumably be explained by the presence of interstitial dopant along with intrinsic interstitial defects of the host matrix. Let us focus attention on the local structure of silicon, the study of which is the aim of this paper. As will be shown later, considering only silicon interstitial atoms during interpretation the Si K edge X-ray absorption spectra would be insufficient to explain the dependences observed in the experimental data, where presumably, at low

$T_s$ , the concentration of substituted silicon atoms, rather than interstitial ones, plays a major role. As  $T_s$  increases, the visible strain from implantation decreases. As mentioned above, after subsequent substrate heating, which is expected to simultaneously perform activation of implanted ions and promote host lattice recovery, the fringes to the left of the main peak diminish. Randomly displaced lattice atoms and extended defects like dislocations and stacking faults affect XRD patterns by either forming fringe patterns on the low-angle side of the diffraction profile or affecting the diffracted beam intensity. The evolution of the average strain maxima in the [201] direction and the static Debye-Waller (DW) factor of  $\beta$ -Ga<sub>2</sub>O<sub>3</sub>:Si samples reveal a moderate decrease in the average strain, accompanied by an increase in DW factor as  $T_s$  increases (Figure 3(b)), reaching 0.8 for  $T_s = 800$  °C. Both parameters were estimated using RadMax software [47], and the obtained results are shown in Figures S2-S3. Nevertheless, the dependencies shown in Figures 1(b) and 3(b) could be associated with a decrease in the overall number of extended defects, such as dislocations and stacking faults, as a function of  $T_s$ , which was further confirmed by TEM studies.

HR XRD results correlate well with RBS/PIXE/c ones presented in Fig. 2. An improvement of channeling as a function of  $T_s$  can clearly be recognized, as the yield dip from the host Ga atoms at  $T_s = 800$  °C compared to  $T_s = 300$  °C is deeper. The normalized yield for the PIXE Si X-ray signal,  $\chi_{Si}$ , for the samples with  $T_s = 700 - 800$  °C is shallower for the [201] direction. Therefore, it can be assumed that not all of the nonrandom silicon atoms are located at Ga substitutional sites, Si<sub>Ga</sub>. This behavior does not rule out the possibility that some of these atoms are at interstitial sites, Si<sub>i</sub>. We assume that a small protrusion into the channel (see Fig. 2 for  $T_s = 700 - 800$  °C) exists so that the yield dip from solute Si

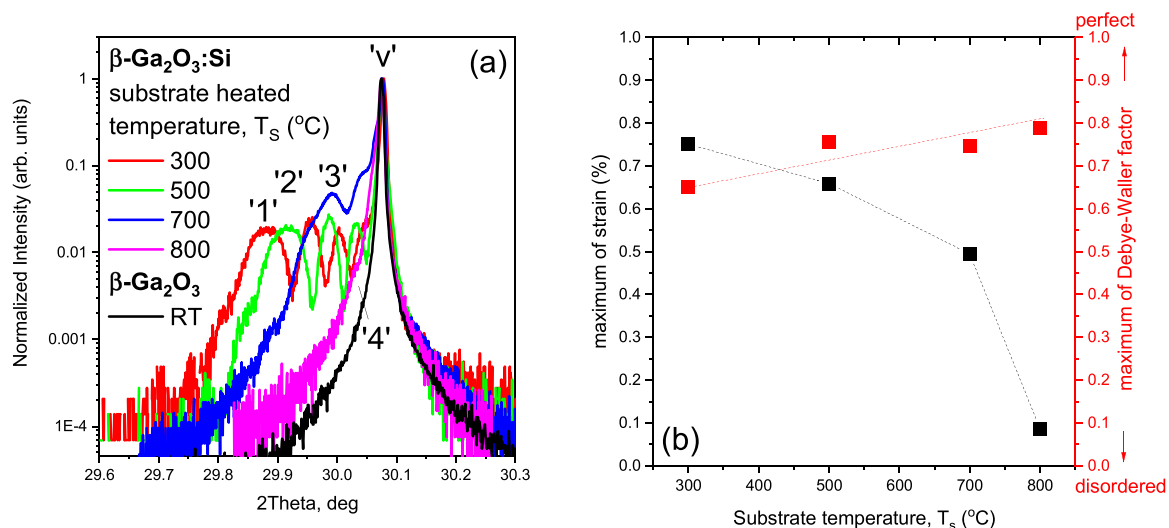
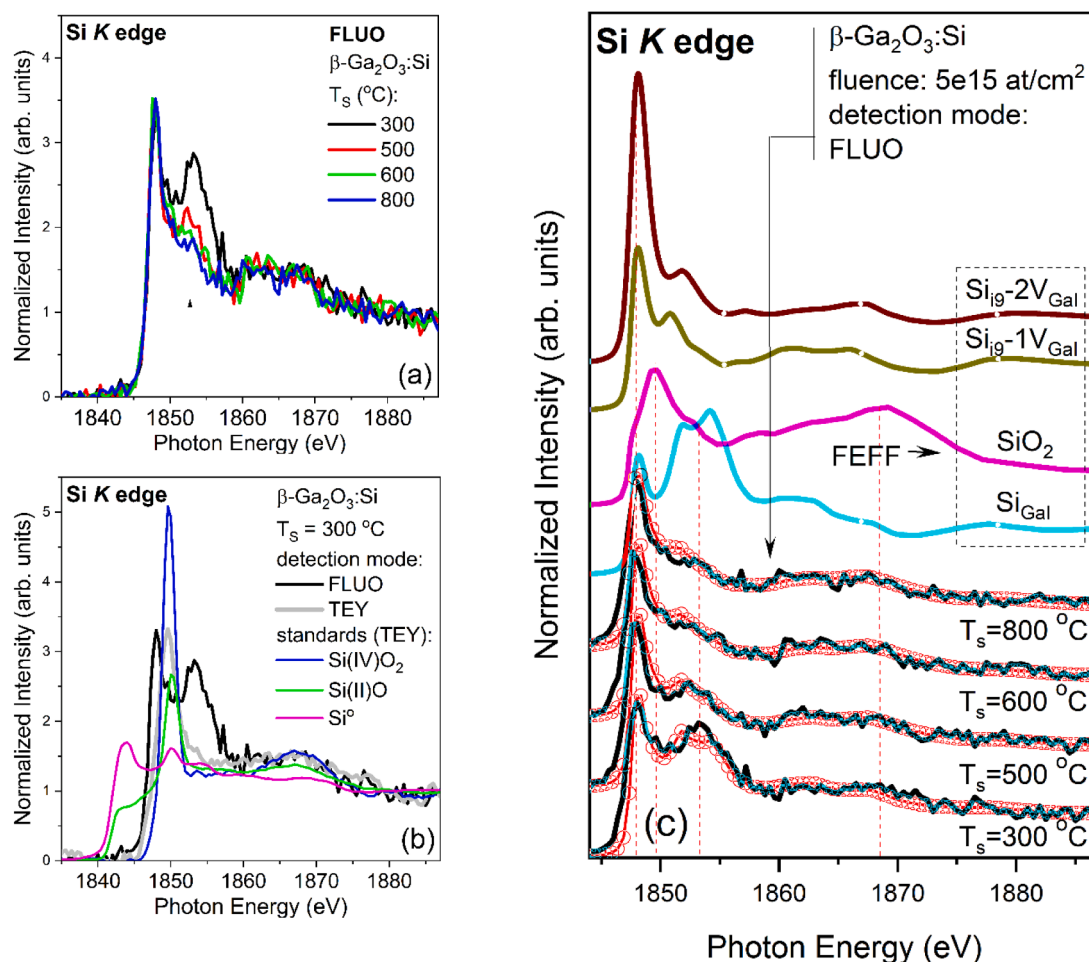


Fig. 3. (a) Measured high-resolution X-ray diffraction (HR-XRD)  $2\theta/\omega$  profiles (XDP), 400 symmetric reflection, of the virgin sample (black line with the substrate peak at  $2\theta \approx 30.075^\circ$  labeled as 'v') and Si implanted  $\beta$ -Ga<sub>2</sub>O<sub>3</sub> under the condition of a heated substrate at 300 °C (red line with the maximum deviation peak at  $2\theta \approx 29.88^\circ$  labeled as '1'), 500 °C (green,  $2\theta \approx 29.92^\circ$ , '2'), 700 °C (blue,  $2\theta \approx 29.99^\circ$ , '3'), and 800 °C (magenta line, '4'). Fringes are clearly visible for the lower substrate temperatures, but only slight strain remains in the sample implanted at the 800 °C substrate temperature. (b) Evolution of the maximum average strain and static Debye-Waller (DW) factor of Ga<sub>2</sub>O<sub>3</sub> samples implanted with Si at different crystal heated temperatures,  $T_s$ .

atoms is narrower than the yield dip from host Ga atoms. In other words, this simply means that the narrower Si scans may come from two sources: interstitials and displaced Si, but they cannot be unambiguously distinguished. This could also be a fingerprint of the complexes of the interstitial  $\text{Si}_{i5,8,9}$  (here, the notation from Shokri et al. is used [48]) with intrinsic point defects like gallium vacancy,  $V_{\text{Ga}}$ , or defects like  $\text{Si}_{\text{Ga}}$ . Oxygen vacancies were excluded from consideration based on the results of DFT simulations obtained under gallium-poor conditions [49]. At this stage, we cannot rule out a situation for which Si signal is a combination of substitutional/interstitial Si plus their small displacement, as case (g) in Figure 15 in [63], since our obtained RBS/PIXE/c results have weak statistics for such analysis. To unambiguously determine whether Si atoms are indeed interstitial, it would be necessary to perform the experiment in a different orientation(s).

As a next step, XANES spectroscopy, which provides insight into the unoccupied electronic states, specifically the density of states near the Fermi level, was applied. XANES helps to obtain critical information on the oxidation state, local geometric and electronic structure, and chemical environment of specific atoms in a material. The normalized XANES spectra of  $\beta\text{-Ga}_2\text{O}_3\text{:Si}$  originating from the transitions of Si 1s core electrons to unoccupied states having *p*-symmetry relative to silicon atoms in the function of  $T_{\text{S}}$  are compared in Fig. 4(a). First, to perform a qualitative analysis, we compare the XANES spectra of  $\beta\text{-Ga}_2\text{O}_3\text{:Si}$  with nanocrystalline silicon,  $\text{SiO}$ , and  $\text{SiO}_2$ , as the fine structure of XANES

reflects the symmetry of the local environment. This allows us to determine the oxidation state of the absorbing atom by identifying shifts in the absorption edge energy of the spectrum. The oxidation state of silicon is the same in all implanted samples and is close to  $4^+$  instead of 0 or  $2^+$ . To distinguish between the ‘surface’ and ‘bulk’ signals from silicon in the  $\beta\text{-Ga}_2\text{O}_3\text{:Si}$  system, TEY and FLUO detection modes [50] were utilized, respectively (Figure 4 (b)). TEY is a surface-sensitive technique, as it detects secondary electrons emitted from the sample, which typically have low kinetic energies. Due to the limited escape depth of such electrons (typically a few nanometers), this detection mode provides information about the near-surface region of the sample. In contrast to TEY, FLUO (or total fluorescence yield (TFY)) is more bulk-sensitive. It detects X-ray fluorescence photons emitted when the material relaxes after absorption. The probing depth in FLUO mode is typically greater, often reaching hundreds of nanometers depending on the material and energy, providing information on the bulk of the sample rather than just the surface. The observed changes in the fine structure of the spectra allowed us to conclude that the local electronic structure around the silicon on the surface of the  $\beta\text{-Ga}_2\text{O}_3\text{:Si}$  differs from the bulk one and is close to  $\text{SiO}_2$ . By performing Si K edge XANES line scanning along the sample’s surface, we found that this phase is randomly distributed. Namely, at different positions of the line scanning, the local structure around silicon was very similar to silicon dioxide. In other positions, the signal remained close to the bulk one, see



**Fig. 4.** (a) Normalized Si K-edge XANES spectra of  $\beta\text{-Ga}_2\text{O}_3\text{:Si}$  in the function of heated substrate temperature,  $T_{\text{S}}$  measured using FLUO detection mode. A 2nd resonance is indicated by the arrow. (b) Normalized Si K-edge XANES spectra of the sample with  $T_{\text{S}} = 300$  °C measured in both detection modes (FLUO vs TEY) and the nanocrystalline silicon,  $\text{SiO}$ , and  $\text{SiO}_2$  standards (only TEY detection mode was used in order to avoid the self-absorption effect). (c) Comparison of theoretical XANES spectra calculated using FEFF with the experimental spectra shown in (a). Black solid lines are the experimental spectra. Other colored solid lines correspond to the spectra of the specific defect complexes. The red circles correspond to a linear combination of the theoretical models. The energy positions of the 1st and 2nd resonances for the  $T_{\text{S}} = 300$  °C sample are 1848 eV and 1853.2 eV, respectively. The two resonances that correspond to  $\text{SiO}_2$  phase are at 1850 eV and 1867 eV.

black/red curves in Figure 4(a), which is in good agreement with the STEM results shown in Fig. 6 (b and c).

To interpret the local atomic structure around the absorber (which is silicon in this case) in greater detail and validate theoretical models, the experimental XANES spectra were compared with simulations using FEFF code. Note that the validity of the model selection to be used for FEFF simulations was determined using DFT calculations, which will be discussed below. FEFF simulations showed that the local structure around silicon, in the context of the positions of two resonances at  $T_S = 300\text{ }^\circ\text{C}$  (1st:1848 and 2nd:1853.2 eV), is described quite well by

substitutional  $\text{Si}_{\text{GaI}}$  in  $\beta\text{-Ga}_2\text{O}_3$  (Figure 4(c)). It should be noted that the fine structure of XANES spectra is reflective of the symmetry of the local environment around the absorber. Sharp, well-defined features may indicate a higher degree of symmetry, whereas broad or asymmetric features may suggest local distortions or defects. The increase in  $T_S$  leads to a slight narrowing of the 1st resonance, which does not contradict RadMaX simulation results, for which the DW factor slightly improves. However, the decrease of the 2nd resonance intensity with  $T_S$  could not be explained by the presence of only a substitutional  $\text{Si}_{\text{GaI}}$  or by some reorganization around this defect. The incorporation of defect

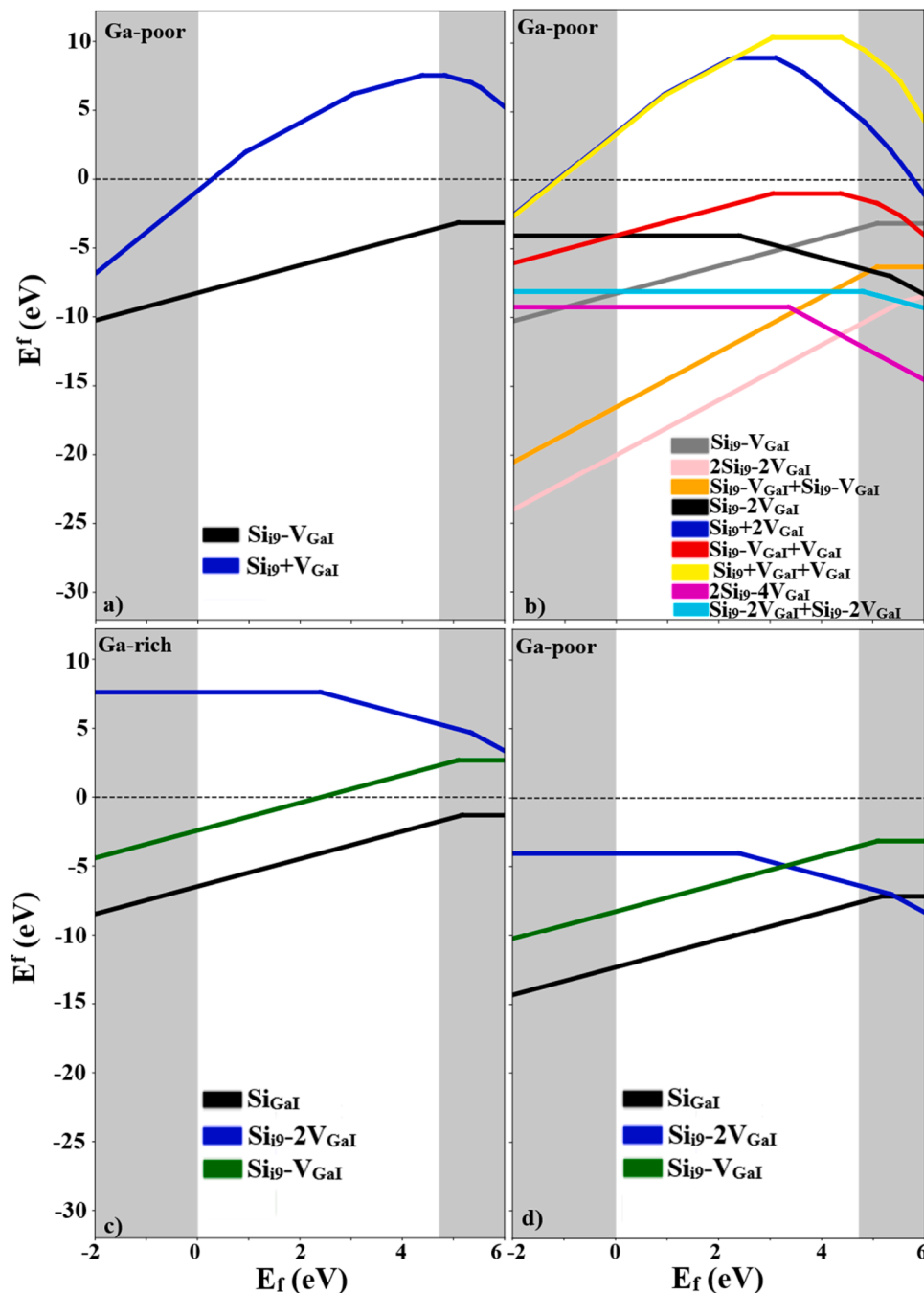


**Fig. 5.** Formation energies  $E^f$  for complexes in  $\beta\text{-Ga}_2\text{O}_3$  plotted against the Fermi energy  $E_f$  for Ga-poor conditions: (a) the  $\text{Si}_{i9-1V_{\text{GaI}}}$  complex and (b) the  $\text{Si}_{i9-2V_{\text{GaI}}}$  complex. In the figures, the formation energy of the complex (marked with “-” sign) is lower than the summation of the formation energies for separate defects (marked with “+” sign) (these partial defects can be  $i9$ ,  $V_{\text{GaI}}$ ,  $2V_{\text{GaI}}$ , and  $i9-V_{\text{GaI}}$ ). Note that the boundaries for the nonshaded region correspond to the valence band maximum (VBM at  $E_f = 0$  eV) and the conduction band minimum (CBM at  $E_f = E_g = 4.73$  eV). For DFT computational details see Supplementary Information. Also note that the same behavior will be observed for Ga-rich conditions, but the values of the formation energy will be shifted by a constant. Formation energies for Si impurity (complexes) in  $\beta\text{-Ga}_2\text{O}_3$ , are plotted against the Fermi energy for (c) Ga-rich and (d) Ga-poor conditions.

complexes consisting of  $\text{Si}_{\text{GaI}}$  with one or more vacancies, either oxygen ( $\text{V}_{\text{OI}}$ ) or gallium ( $\text{V}_{\text{GaI}}$ ), in the consideration, did not result in the disappearance of the 2nd resonance. In addition, two relatively intense states around 1850 and 1867 eV are clearly missing in the theoretical spectra of the  $\text{Si}_{\text{GaI}}$  model. Both are well accounted for by the  $\text{SiO}_2$  phase states. Consequently, we cannot rule out the presence of small, randomly distributed  $\text{SiO}_2$  regions in the sample volume. A similar phenomenon was observed in  $\beta\text{-Ga}_2\text{O}_3$  ( $\bar{2}01$ ) implanted by Si at a fluence  $2e^{16}$   $\text{Si}/\text{cm}^2$  [40], where the electron energy loss spectroscopy technique was employed instead of XANES. Hence, an alternative explanation satisfying the description of the FLUO Si K edge XANES spectra must be sought.

Despite extensive research on  $\beta\text{-Ga}_2\text{O}_3\text{:Si}$ , a comprehensive study of the various possible Si defects other than substitutional ones is still lacking. One of the reasons for this is that in a thermodynamically stable condition, the formation energy of  $\text{Si}_{\text{Ga}}$  is much lower than that of  $\text{Si}_i$  [48,51,52], and therefore, only a small concentration of interstitials is expected to be present in a sample [48,53]. However, when a suitable out-of-equilibrium modification technique such as ion implantation doping is used, due to the ballistic nature of this process, the build-up of

a lattice disorder occurs, accompanied by the formation of various types of defects, including interstitials. In consideration of the aforementioned details, the complexes of  $\text{Si}_i$  with one or two cation vacancies were also considered. As shown in previous studies [41,42], the proposed divacancy-cation interstitial complexes correlate directly with the structures obtained by DFT, which predicts that they are compensating acceptors in  $\beta\text{-Ga}_2\text{O}_3$ . In turn, the positron annihilation spectroscopy data were interpreted as the signals being dominated by split  $\text{V}_{\text{Ga}}$  defects in  $\beta\text{-Ga}_2\text{O}_3$  [43]. Theory predicts that the split Ga vacancy configuration has low formation energy (see also Figure S4(b)), and EPR, IR, STEM experiments agree that such a configuration is the most likely interpretation [43]. Consequently, in addition to the identified most favorable  $\text{Si}_i$  sites by calculating their formation energy [48], we also considered their complexes with one or two closest  $\text{V}_{\text{Ga}}$  (Fig. 5). Such a possibility seems to be even more realistic since the process of implantation into  $\beta\text{-Ga}_2\text{O}_3$  (100) under heated substrate conditions was carried out for about 8 h and was motivated by the absence of mechanical degradation of the host crystal in this way.

Here, we selected an interstitial Si at sites 5, 8 and 9, i.e.,  $\text{Si}_{i5,8,9}$ , due to their lowest formation energy amongst other interstitials [48]. As can

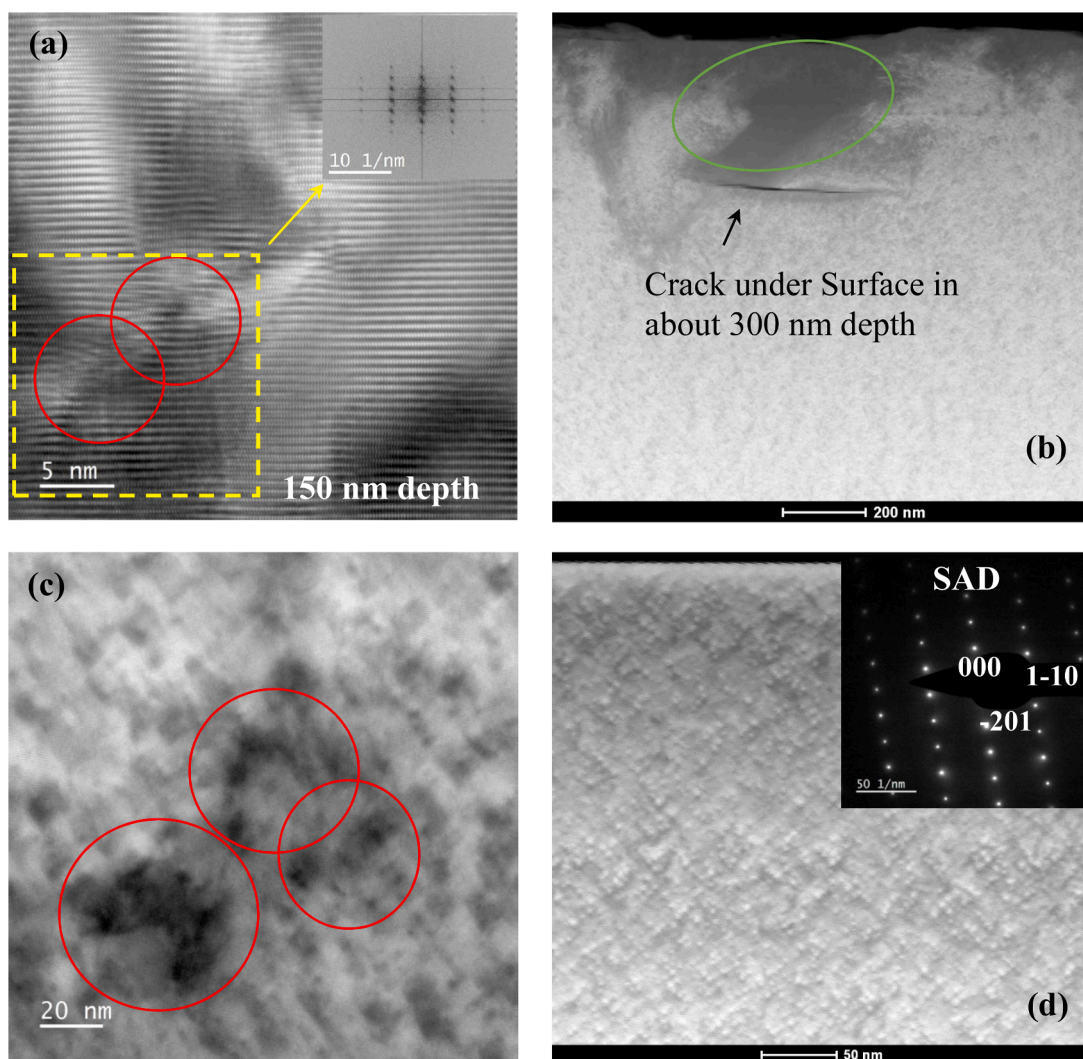


**Fig. 6.** (a) HR-TEM image of (100)  $\beta\text{-Ga}_2\text{O}_3\text{:Si}$  at  $T_S = 400$  °C, taken 150 nm below the surface along the [010] direction, highlighting pronounced extended defects but no evidence of secondary phases (FFT inset). (b) STEM overview of (100)  $\beta\text{-Ga}_2\text{O}_3\text{:Si}$  implanted at  $T_S = 400$  °C, revealing near-surface damage, including a visible crack. The darker contrast suggests the possible presence of  $\text{SiO}_2$ , which has a lower density and atomic number than  $\text{Ga}_2\text{O}_3$ . (c) HR-TEM image of (100)  $\beta\text{-Ga}_2\text{O}_3\text{:Si}$  at  $T_S = 600$  °C, also along [010], showing darker nano-regions, likely indicative of a higher silicon concentration, either in complex formations or as  $\text{SiO}_2$ , as inferred from TEM Brightfield analysis. (d) STEM overview of (100)  $\beta\text{-Ga}_2\text{O}_3$  implanted at  $T_S = 800$  °C, displaying no detectable secondary phases (SAD inset), though nano-voids are presumably present [57].

be seen in Figure S5, the presence of the  $\text{Si}_{i5}-2\text{V}_{\text{GaI}}$  or  $\text{Si}_{i9}-2\text{V}_{\text{GaI}}$  complexes introduces localized electronic states within the band gap:  $\varepsilon(2-/0)$  at 3.662 and  $\varepsilon(1-/0)$  at 2.405 eV with respect to the valence band maximum, respectively. The model containing  $\text{Si}_{i8}$  was discarded due to the impossibility of forming a complex linking between the  $\text{Si}_{i8}$  atom and the two nearest  $\text{Ga}_I$  vacancies. For the complex  $\text{Si}_{i9}-2\text{V}_{\text{GaI}}$ , the transition level  $\varepsilon(2-/1-)$  is in the conduction band, see Figure 5(d). This complex may act as trap levels for electrons, influencing n-type conductivity negatively. Our findings correlate well with the conclusions presented in Johnson et al. [42]. Significantly higher values of the formation energy estimated for the complex  $\text{Si}_{i5}-2\text{V}_{\text{GaI}}$  compared to  $\text{Si}_{i9}-2\text{V}_{\text{GaI}}$  allowed us to exclude it from further analysis of Si K edge XANES data (see Figure S5). The considered  $\text{Si}_{i9}-2\text{V}_{\text{GaI}}$  complex can be obtained by attracting  $\text{V}_{\text{GaI}}$  towards  $\text{Si}_{i9}$ , so the formation energy of the  $\text{Si}_{i9}-1\text{V}_{\text{GaI}}$  complex was estimated. This complex introduces a localized electronic state within the conduction band ( $\varepsilon(1/0)$ ) at 0.358 eV with respect to the conduction band minimum, see Figure 5(d). The energy of its formation is higher the energy of  $\text{Si}_{\text{GaI}}$  formation, but, considering the above-mentioned non-equilibrium process during implantation, the formation of such a complex cannot be excluded. The complexes of  $\text{Si}_i$  with one or two  $\text{Si}_{\text{GaI}}$  were also tested to understand the possible interstitial/substitutional Si atom clustering. The analysis revealed that both are donors but do not prefer to form (Figure S6), consequently, these complexes were not considered in the following analysis. With the above considerations, we proceeded to interpret the XANES data.

Figure 4(c) compares the theoretical Si K edge XANES spectra for the models selected by DFT (shown in Fig. 5) with a group of experimental spectra at different  $T_S$ . A qualitative analysis of the spectra indicates (i) the presence of randomly distributed regions of  $\text{SiO}_2$  (Figure 4(b)), (ii) a decrease in the number of  $\text{Si}_{\text{GaI}}$ , and (iii) a simultaneous increase in the number of complexes including  $\text{Si}_i$  with increasing  $T_S$ . To achieve the best agreement between theory and experiment, the previously described approach [54] was used, in which linearized combinations of the calculated spectra with different weighting factors were constructed. The differential evolution procedure was employed as a minimization procedure to identify the optimal model weighting coefficients [55]. Table 1 presents the models with their estimated weights, and the spectra obtained by a linear combination routine are marked as red open circles in Figure 4(c). It should be noted that this procedure provides a very rough estimate of the weights, offering only a numerical trend, as the theory itself has limitations in accurately calculating the intensity of the resonances. Despite this limitation, we assume that such an estimate allows to trace the dependence observed in the experiment in more detail. First, as seen in Table 1, it is observed that the number of silicon atoms representing  $\text{SiO}_2$  nano-inclusions remains nearly constant across all  $T_S$ , indicating that it does not depend on the substrate temperature during implantation. The same is true for the complex  $\text{Si}_{i9}-2\text{V}_{\text{GaI}}$ . On the other hand, the weight of the complex  $\text{Si}_{i9}-1\text{V}_{\text{GaI}}$  is zero for  $T_S=300^\circ\text{C}$ ; it increases and remains nearly constant for  $T_S=500-600^\circ\text{C}$ , reaching a

**Table 1**

Results of a linear combination of theoretical Si K edge XANES spectra obtained using the differential evolution procedure: weights (left value) vs. at % (right value) for a defect/complex, reported together with  $\sigma^2$ , which is a measure of the mean square of the discrepancy between the calculated and experimental values at each data point. It should be noted that this procedure results in a rough estimate of the weights, providing only a numerical trend, given the discrepancy between theory and experiment in the context of the intensity of the calculated resonances. Here,  $\text{Si}_{\text{GaI}}$  denotes substitutional Si at the  $\text{Ga}_I$  site,  $\text{V}_{\text{GaI}}$  refers to a gallium vacancy at the  $\text{Ga}_I$  site, and  $\text{Si}_{i9}$  represent interstitial Si defects. The notation for interstitial defect position follows [48].

$T_S, ^\circ\text{C}$	$\text{Si}_{\text{GaI}}$	$\text{Si}_{i9}-1\text{V}_{\text{GaI}}$	$\text{Si}_{i9}-2\text{V}_{\text{GaI}}$	$\text{SiO}_2$	$\sigma^2$
300	0.49/0.10	0.00/0.00	0.24/0.05	0.27/0.05	0.051
500	0.26/0.05	0.07/0.01	0.32/0.06	0.34/0.07	0.047
600	0.20/0.04	0.10/0.02	0.32/0.06	0.38/0.08	0.047
800	0.14/0.03	0.23/0.05	0.28/0.06	0.34/0.07	0.042

maximum value of about 0.05 at % for  $T_S=800^\circ\text{C}$ . In contrast, the number of  $\text{Si}_{\text{GaI}}$  decreases with increasing  $T_S$ . Let us point out that according to our DFT calculations (Figure S4(a)),  $\text{Si}_{\text{GaI}}$  defects do not preferentially form complexes like  $\text{Si}_{\text{GaI}}-\text{Si}_{\text{GaI}}$ .

Figures S7-S8 illustrate the relaxed structures of the considered models with complexes after the relaxation procedure. Interstitial silicon atom belonging to a complex with one vacancy is displaced into the channels along [201] direction more strongly than in case of the  $\text{Si}_{i9}-2\text{V}_{\text{GaI}}$  complex. Furthermore, the  $\text{Si}_{i9}-2\text{V}_{\text{GaI}}$  complexes attract each other (Figure 5(b)). Consequently, if the  $\text{Si}_{i9}-2\text{V}_{\text{GaI}} - \text{Si}_{i9}-2\text{V}_{\text{GaI}}/(\text{Si}_{i9}-1\text{V}_{\text{GaI}} - \text{Si}_{i9}-1\text{V}_{\text{GaI}})$  complexes are attracted, the silicon atoms belonging to these complexes are 'screened'/'(non screened)' by the host matrix atoms, rendering them 'invisible'/'(visible)' to the Si PIXE/c along the [201] direction, respectively (see Figure S8). Based on the data reported in Figures 5(b) and S7-8, we can assume that the channel yields of Si revealed in the PIXE/c angular distributions spectra in [201] direction shown in Fig. 2 most likely represent silicon atoms bound to the  $\text{Si}_{i9}-1\text{V}_{\text{GaI}}$  complex and the silicon dioxide nano-inclusions. Considering the above, it is also logical to assume that a larger number of the considered complexes may lead to the formation of nano-voids in the host matrix. Moreover, we attribute the discrepancy between the presence of interstitial Si atoms in the system with  $T_S = 400 - 600^\circ\text{C}$ , as determined by Si K edge XANES analysis and presented in Table 1, and their absence in the RBS/PIXE/c measurements compared to  $T_S = 700 - 800^\circ\text{C}$  data, as observed in Fig. 2, to the influence of the mosaicity of the system under study on RBS/PIXE channeling measurements. This phenomenon was investigated by De Vries, who concluded that mosaicity influences the channeling profiles, causing them to broaden and become less intense [56]. Thus, the data presented in Table 1 do not contradict the RBS/PIXE/c studies. The results presented in Table 1 demonstrate that among the samples studied, the substrate temperature  $T_S = 800^\circ\text{C}$  during the implantation is optimal in terms of crystallographic properties. Firstly, HR XRD studies revealed that this sample exhibited the lowest structural disorder and strain levels. Secondly, TEM analysis indicated the lowest number of extended defects in this sample. Furthermore, the analysis of the Si K edge XANES data, in conjunction with DFT calculations, showed that for this sample, excluding the parasitic randomly distributed  $\text{SiO}_2$  nano-inclusions, approximately 60 % of the silicon atoms are involved in complexes that act as donors, promoting n-type conduction. However, approximately 40 % of the implanted silicon atoms form complexes that act as traps for conduction electrons. Notably, in addition to the  $\text{Si}_{\text{GaI}}$  atoms discussed previously in the literature, the  $\text{Si}_i$  atoms in complexes investigated in the present work also contribute to n-type conduction. The number of interstitial Si atoms positively contributing to the n-type conductivity is approximately twice as large as the substituted ones.

TEM analysis revealed a significant change in the distribution of the  $\text{SiO}_2$  phase in samples implanted at higher temperatures ( $T_S = 600, 800^\circ\text{C}$ ) compared to  $T_S = 300^\circ\text{C}$ . The fast Fourier transform (FFT) analysis of the highlighted area in Figure 6(a) shows only  $\beta$ -phase. STEM analysis of the sample with  $T_S = 800^\circ\text{C}$  shows significantly less damage, which agrees well with XRD, RBS/PIXE/c, and Si K edge XANES data analysis, with no direct observation of extended defects such as dislocations. Moreover, selected area diffraction (SAD) analysis (Figure 6(d)) shows no second phases. To understand the presence of numerous light spots visible in Figure 6(d) for the sample with the highest  $T_S$ , we referred to the HAADF-STEM study [57], where the observed nano-sized voids were retained within the  $\beta\text{-Ga}_2\text{O}_3$  structure due to high-temperature annealing during (or after) ion implantation. Such an effect has been observed and extensively discussed in the literature, for example, in the GaAs:Mn system [58,59]. The existence of the  $\gamma$ -phase [57,60] and the formation of nano-voids [57] are both plausible and documented phenomena resulting from ion implantation. The predominance of one over the other can depend on specific experimental conditions like ion dose, energy, and annealing parameters. Due to the fundamental nature of defect aggregation under high-energy conditions, the formation of

nano-voids is a more universally accepted and observed phenomenon across various materials subjected to ion implantation. Nevertheless, the stabilization of the  $\gamma$ -phase is more specific to  $\beta$ -Ga<sub>2</sub>O<sub>3</sub> and its unique response to implantation and annealing conditions [60]. Consequently, considering that the implantation process took 8 h to deliver the necessary amount of the dopant content and to avoid mechanical destruction of the  $\beta$ -Ga<sub>2</sub>O<sub>3</sub> (100) surface, we are more inclined to assume that revealed spots represent nano-voids rather than Si-rich, SiO<sub>2</sub>, or  $\gamma$ -phase inclusions.

#### 4. Conclusions

Our investigation confirms that the high-temperature implantation parameters employed do not induce mechanical degradation of the sample surface. By utilizing complementary XRD, XANES, RBS/PIXE/c, and TEM analyses, we examine lattice deformation, identify the local environment of dopants, and assess local structure modifications, including the presence of extended defects such as edge dislocations and stacking faults resulting from ion bombardment onto the heated substrate. Comprehensive analysis of the data reveals the existence of defect/complexes such as Si<sub>Gal</sub>, Si<sub>i9</sub>-1V<sub>Gal</sub>, and Si<sub>i9</sub>-2V<sub>Gal</sub>, as well as the presence of the SiO<sub>2</sub> phase. DFT calculations support the experimental findings, confirming that all considered complexes, except Si<sub>i9</sub>-2V<sub>Gal</sub>, act as donors, positively influencing n-type conductivity. Notably, no  $\beta$ -phase transformation was observed during implantation, even at the lowest substrate temperature. The formation of nano-voids in the sample implanted at T<sub>S</sub> = 800 °C is presumably the result of the interplay between defect creation, migration, and aggregation. A detailed understanding of these mechanisms is necessary to optimize implantation processes and improve the properties of implanted  $\beta$ -Ga<sub>2</sub>O<sub>3</sub> (100).

#### CRedit authorship contribution statement

**I.N. Demchenko:** Writing – review & editing, Visualization, Software, Investigation, Formal analysis, Conceptualization. **Y. Syryanny:** Writing – review & editing, Software, Formal analysis. **A. Shokri:** Writing – review & editing, Visualization, Software, Formal analysis. **Y. Melikhov:** Writing – review & editing, Investigation, Formal analysis. **J. Domagała:** Data curation. **R. Minikayev:** Data curation. **A. Derkachova:** Data curation. **F. Munnik:** Data curation. **U. Kentsch:** Data curation. **M. Zajac:** Data curation. **A. Reck:** Data curation, Formal analysis. **N. Haufe:** Data curation. **Z. Galazka:** Writing – review & editing, Conceptualization.

#### Declaration of competing interest

The authors declare that they have no known competing financial interests or personal relationships that could have appeared to influence the work reported in this paper.

#### Acknowledgments

These studies were financially supported by the project UMO-2020/39/B/ST5/03580 funded by the National Science Centre (NCN) in Poland. The work was partially supported by the Interdisciplinary Centre for Mathematical and Computational Modelling (ICM) at University of Warsaw, Poland, grant ID 3557. We gratefully acknowledge Poland's high-performance Infrastructure PLGrid (HPC Centers: ACK Cyfronet AGH, PCSS, CI TASK, WCSS) for providing computer facilities and support within computational grant no PLG/2023/016578. This publication was partially developed under the provision of the Polish Ministry and Higher Education project "Support for research and development with the use of research infrastructure of the National Synchrotron Radiation Centre SOLARIS" under contract no 1/SOL/2021/2. We acknowledge SOLARIS Centre for the access to the PIRX beamline, where the measurements were performed. RBS/c and PIXE/c

were carried out at IBC at the Helmholtz-Zentrum Dresden-Rossendorf e. V., funded by the EU's Horizon 2020 programme under grant agreement No 824096. TEM analysis was financed by Ascent+ European Union's Horizon 2020 research and innovation program under GA No 871130. We would like to thank A. Azarov of the University of Oslo, Centre for Materials Science and Nanotechnology, Norway, and K. M. Yu of Lawrence Berkeley National Lab, USA, for fruitful discussions. The authors thank Andreas Fiedler (Leibniz-Institut für Kristallzüchtung) for critical reading of the paper. Bulk crystal growth and wafer preparation were financially supported by the Federal Ministry of Education and Research (BMBF, Germany) under grant number 16ES1084K.

#### Data availability

The data that support the findings of this study are publicly available at <https://doi.org/10.18150/CYIRAU>.

#### Declaration of generative AI and AI-assisted technologies in the writing process

During the preparation of this article, the authors used DeepL to improve language and readability. After using this service, the authors revised and edited the content as necessary and are fully responsible for the content of the publication.

#### Supplementary materials

Supplementary material associated with this article can be found, in the online version, at [doi:10.1016/j.actamat.2025.121036](https://doi.org/10.1016/j.actamat.2025.121036).

#### References

- [1] A. Kuramata, K. Koshi, S. Watanabe, Y. Yamaoka, T. Masui, S. Yamakoshi, High-quality  $\beta$ -Ga<sub>2</sub>O<sub>3</sub> single crystals grown by edge-defined film-fed growth, *Jpn. J. Appl. Phys.* 55 (2016) 1202A2.
- [2] Z. Galazka, Growth of bulk  $\beta$ -Ga<sub>2</sub>O<sub>3</sub> single crystals by the Czochralski method, *J. Appl. Phys.* 131 (2022) 031103.
- [3] K. Hoshikawa, T. Kobayashi, E. Ohba, T. Kobayashi, 50mm diameter Sn-doped (001)  $\beta$ -Ga<sub>2</sub>O<sub>3</sub> crystal growth using the vertical bridgeman technique in ambient air, *J. Cryst. Growth* 546 (2020) 125778.
- [4] A. Kuramata, K. Koshi, S. Watanabe, Y. Yamaoka, Floating zone method, edge-defined film-fed growth method, and wafer manufacturing, in: M. Higashiwaki, S. Fujita (Eds.), Gallium Oxide: Crystal Growth, Materials Properties, and Devices, Springer Nature, 2020, pp. 57–75.
- [5] G. Janowitz, V. Scherer, M. Mohamed, A. Krapf, H. Dwelk, R. Manzke, Z. Galazka, R. Uecker, K. Irmscher, R. Fornari, M. Michling, D. Schmeißer, J.R. Weber, J. R. Varley, C.G. Van de Walle, Experimental electronic structure of In<sub>2</sub>O<sub>3</sub> and Ga<sub>2</sub>O<sub>3</sub>, *New. J. Phys.* 13 (2011) 085014.
- [6] F. Alema, A. Osinsky, N. Orishchin, N. Valente, Y. Zhang, A. Mauze, J.S. Speck, Low 114 cm<sup>-3</sup> free carrier concentration in epitaxial  $\beta$ -Ga<sub>2</sub>O<sub>3</sub> grown by MOCVD, *APL Mater.* 8 (2020) 021110.
- [7] F. Alema, T. Itoh, S. Vogt, J.S. Speck, A. Osinsky, Highly conductive epitaxial  $\beta$ -Ga<sub>2</sub>O<sub>3</sub> and  $\beta$ -(Al<sub>x</sub>Ga<sub>1-x</sub>)<sub>2</sub>O<sub>3</sub> films by MOCVD, *Jpn. J. Appl. Phys.* 61 (2022) 100903.
- [8] L. Meng, Z. Feng, A.F.M.A.U. Bhuiyan, H. Zhao, High-mobility MOCVD  $\beta$ -Ga<sub>2</sub>O<sub>3</sub> epitaxy with fast growth rate using trimethylgallium, *Cryst. Growth* 22 (2022) 3896.
- [9] M. Higashiwaki, K. Sasaki, A. Kuramata, T. Masui, S. Yamakoshi, Gallium oxide (Ga<sub>2</sub>O<sub>3</sub>) metal-semiconductor field-effect transistors on single-crystal  $\beta$ -Ga<sub>2</sub>O<sub>3</sub> (010) substrates, *Appl. Phys. Lett.* 100 (2012) 013504.
- [10] S. Pearton, in: F. Ren M. Mastro (Ed.), Gallium Oxide: Technology, Devices and Applications, Elsevier, 2019.
- [11] M. Higashiwaki, in: S. Fujita (Ed.), Gallium Oxide: Materials Properties, Crystal Growth, and Devices, Springer Nature Switzerland AG, 2020.
- [12] M.H. Wong, K. Goto, H. Murakami, Y. Kumagai, M. Higashiwaki, Current aperture vertical  $\beta$ -Ga<sub>2</sub>O<sub>3</sub> MOSFETs fabricated by N- and Si-ion implantation doping, *IEEE Electron. Device Lett.* 40 (2019) 431.
- [13] K. Sasaki, M. Higashiwaki, A. Kuramata, T. Masui, S. Yamakoshi, Si-ion implantation doping in  $\beta$ -Ga<sub>2</sub>O<sub>3</sub> and its application to fabrication of low-resistance ohmic contacts, *Appl. Phys. Express* 6 (2013) 086502.
- [14] J.A. Spencer, M.J. Tadjer, A.G. Jacobs, M.A. Mastro, J.L. Lyons, J.A.Jr. Freitas, J. C. Gallagher, Q.T. Thieu, K. Sasaki, A. Kuramata, Y. Zhang, T.J. Anderson, K. D. Hobart, Activation of implanted Si, Ge, and Sn donors in high-resistivity halide vapor phase epitaxial  $\beta$ -Ga<sub>2</sub>O<sub>3</sub>:n with high mobility, *Appl. Phys. Lett.* 121 (2022) 192102.

- [15] A. Sardar, T.I. Smith, J. Lawson, T. Asel, R.B. Comes, J.N. Merrett, S. Dhar, High conductivity  $\beta$ -Ga<sub>2</sub>O<sub>3</sub> formed by hot Si ion implantation, *Appl. Phys. Lett.* 121 (2022) 262101.
- [16] K. Tetzner, A. Thies, P. Seyidov, T.S. Chou, J. Rehm, I. Ostermayr, Z. Galazka, A. Fiedler, A. Popp, J. Würfl, O. Hilt, Ge-ion implantation and activation in (100)  $\beta$ -Ga<sub>2</sub>O<sub>3</sub> for ohmic contact improvement using pulsed rapid thermal annealing, *J. Vac. Sci. Technol.* 41 (2023) 043102.
- [17] M.H. Wong, C.H. Lin, A. Kuramata, S. Yamakoshi, H. Murakami, Y. Kumagai, M. Higashiwaki, Acceptor doping of  $\beta$ -Ga<sub>2</sub>O<sub>3</sub> by Mg and N ion implantations, *Appl. Phys. Lett.* 113 (2018) 102103.
- [18] K. Tetzner, A. Thies, E.B. Treidel, F. Brunner, G. Wagner, J. Würfl, Selective area isolation of  $\beta$ -Ga<sub>2</sub>O<sub>3</sub> using multiple energy nitrogen ion implantation, *Appl. Phys. Lett.* 113 (2018) 172104.
- [19] R. Schewski, K. Lion, A. Fiedler, C. Wouters, A. Popp, S.V. Levchenko, T. Schulz, M. Schmidbauer, S. Bin Anooz, R. Grüneberg, Z. Galazka, G. Wagner, K. Irmscher, M. Scheffler, C. Draxl, M. Albrecht, Step-flow growth in homoepitaxy of  $\beta$ -Ga<sub>2</sub>O<sub>3</sub> (100) – The influence of the miscut direction and faceting, *APL Mater.* 7 (2019) 022515.
- [20] T.S. Chou, P. Seyidov, S. Bin Anooz, R. Grüneberg, J. Rehm, T.T.V. Tran, A. Fiedler, K. Tetzner, Z. Galazka, M. Albrecht, A. Popp, High-mobility 4  $\mu$ m MOVPE-grown (100)  $\beta$ -Ga<sub>2</sub>O<sub>3</sub> film by parasitic particles suppression, *Jpn. J. Appl. Phys.* 62 (2023) SF1004.
- [21] A.J. Green, K.D. Chabak, E.R. Heller, R.C. Jr. Fitch, M. Baldini, A. Fiedler, K. Irmscher, G. Wagner, Z. Galazka, S.E. Tetlak, A. Crespo, K. Leedy, G.H. Jessen, 3.8-MV/cm breakdown strength of MOVPE-grown Sn-doped  $\beta$ -Ga<sub>2</sub>O<sub>3</sub> MOSFETs, *IEEE Electron. Device Lett.* 37 (2016) 902.
- [22] K. Tetzner, M. Klusch, A. Popp, S. Bin Anooz, T.S. Chou, Z. Galazka, K. Ickert, M. Matala, R.S. Unger, E.B. Treidel, M. Wolf, A. Trampert, J. Würfl, O. Hilt, Enhancement-mode vertical (100)  $\beta$ -Ga<sub>2</sub>O<sub>3</sub> FinFETs with an average breakdown strength of 2.7 MV cm<sup>-1</sup>, *Jpn. J. Appl. Phys.* 62 (2023) SF1010.
- [23] Z. Galazka, R. Uecker, D. Klimm, K. Irmscher, M. Naumann, M. Pietsch, A. Kwasniewski, R. Bertram, S. Ganschow, M. Bickermann, Scaling-up of bulk  $\beta$ -Ga<sub>2</sub>O<sub>3</sub> single crystals by the Czochralski method, *ECS. J. Solid. State. Sci. Technol.* 6 (2017) Q3007.
- [24] J.J. Kas, F.D. Vila, J.J. Rehr, The FEFF code (ch. 6.8), in: C.T. Chantler, F. Boscherini, B. Bunker (Eds.), *International Tables for Crystallography*, International Tables for Crystallography, vol. I, Wiley, 2020, pp. 764–769.
- [25] G. Kresse, J. Hafner, Ab initio molecular-dynamics simulation of the liquid-metal–Amorphous-semiconductor transition in Germanium, *Phys. Rev. B* 49 (1994) 14251.
- [26] G. Kresse, J. Furthmüller, Efficiency of ab-initio total energy calculations for metals and semiconductors using a plane-wave basis set, *Comput. Mater. Sci.* 6 (1996) 15.
- [27] G. Kresse, J. Furthmüller, Efficient iterative schemes for ab initio total-energy calculations using a plane-wave basis set, *Phys. Rev. B* 54 (1996) 11169.
- [28] G. Kresse, D. Joubert, From Ultrasoft pseudopotentials to the projector augmented-wave method, *Phys. Rev. B* 59 (1999) 1758.
- [29] J. Heyd, G.E. Scuseria, M. Ernzerhof, Hybrid functionals based on a screened coulomb potential, *J. Chem. Phys.* 118 (2003) 8207.
- [30] C. Freysoldt, B. Grabowski, T. Hickel, J. Neugebauer, G. Kresse, A. Janotti, C. G. Van de Walle, First-principles calculations for point defects in solids, *Rev. Mod. Phys.* 86 (2014) 253–305.
- [31] C. Freysoldt, J. Neugebauer, C.G. Van de Walle, Electrostatic interactions between charged defects in supercells, *Physica Status Solidi (b)* 248 (2011) 1067.
- [32] M. Passlack, N.E.J. Hunt, E.F. Schubert, G.J. Zyzdzik, M. Hong, J.P. Mannaerts, R. L. Opila, R.J. Fischer, Dielectric properties of electron-beam deposited Ga<sub>2</sub>O<sub>3</sub> films, *Appl. Phys. Lett.* 64 (1994) 2715.
- [33] A. Kyrtsos, M. Matsubara, E. Bellotti, On the feasibility of P-type Ga<sub>2</sub>O<sub>3</sub>, *Appl. Phys. Lett.* 112 (2018) 32108.
- [34] L. Ankudinov, B. Ravel, J.J. Rehr, S.D. Conradson, Real-space multiple-scattering calculation and interpretation of x-ray-absorption near-edge structure, *Phys. Rev. B* 58 (1998) 7565.
- [35] H. Modrow, S. Bucher, J.J. Rehr, A.L. Ankudinov, Calculation and interpretation of k-shell x-ray absorption near-edge structure of transition metal oxides, *Phys. Rev. B* 67 (2003) 035123.
- [36] I.N. Demchenko, J.D. Denlinger, M. Chernyshova, K.M. Yu, D.T. Speaks, P. Olalde-Velasco, O. Hemmers, W. Walukiewicz, A. Derkachova, K. Lawniczak-Jablonska, Full multiple scattering analysis of XANES at the CdL<sub>3</sub> and ok edges in CdO films combined with a soft-x-ray emission investigation, *Phys. Rev. B* 82 (2010) 075107.
- [37] K. Gärtner, Modified master equation approach of axial dechanneling in perfect compound crystals, *Nucl. Instrum. Meth. Phys. Res. B* 227 (2005) 522–530.
- [38] J.F. Ziegler, SRIM – The Stopping and Range of Ions in Matter Software, v.13, 2024. [www.srim.org](http://www.srim.org) (accessed on October 7).
- [39] L.C. Feldman, J.W. Mayer, S.T. Picraux, *Materials Analysis by Ion Channeling: Submicron Crystallography*, Academic Press, New York, 1982.
- [40] S.B. Kjeldby, A. Azarov, P.D. Nguyen, V. Venkatachalapathy, R. Mikšová, A. Macková, A. Kuznetsov, Ø. Prytz, L. Vines, Radiation-induced defect accumulation and annealing in Si-implanted gallium oxide, *J. Appl. Phys.* 131 (2022) 125701.
- [41] J.M. Johnson, Z. Chen, J.B. Varley, C.M. Jackson, E. Farzana, Z. Zhang, A. R. Arehart, H.L. Huang, A. Genc, S.A. Ringel, C.G. Van de Walle, D.A. Muller, J. Hwang, Unusual formation of point-defect complexes in the ultrawide-band-gap semiconductor  $\beta$ -Ga<sub>2</sub>O<sub>3</sub>, *Phys. Rev. X* 9 (2019) 041027.
- [42] J. Johnson, H.L. Huang, J. Hwang, Point defects and complexes in gallium oxide materials and devices, *Microsc. Microanal.* 26 (2020) 838.
- [43] F. Tuomisto, Ga vacancies in  $\beta$ -Ga<sub>2</sub>O<sub>3</sub>: split or not? *Jpn. J. Appl. Phys.* 62 (2023) SF802.
- [44] P.F. Fewster, *X-Ray Scattering from Semiconductors*, Imperial College Press, 2003.
- [45] D.R. Pereira, S. Magalhães, C. Díaz-Guerra, M. Peres, J.G. Correia, J.G. Marques, A. G. Silva, E. Alves, S. Cardoso, P.P. Freitas, K. Lorenz, Estimating the uncertainties of strain and damage analysis by X-ray diffraction in ion implanted MoO<sub>3</sub>, *Nucl. Instrum. Meth. Phys. Res. B* 478 (2020) 290.
- [46] C. Calabretta, M. Zimbone, E.G. Barbaggioanni, S. Boninelli, N. Piluso, A. Severino, M.A. di Stefano, S. Lorenti, L. Calcagno, F. La Via, Thermal annealing of high dose P implantation in 4H-SiC, *Mater. Sci. Forum Fam. Plan. West Hemisph.* 963 (2019) 399.
- [47] M. Souilah, A. Boule, A. Debelle, RadMaX: a graphical program for the determination of strain and damage profiles in irradiated crystals, *J. Appl. Crystallogr.* 49 (2016) 311.
- [48] A. Shokri, Y. Melikhov, Y. Syryanyy, I.N. Demchenko, Point defects in silicon-doped  $\beta$ -Ga<sub>2</sub>O<sub>3</sub>: hybrid-DFT calculations, *ACS Omega (Westport)* 8 (2023) 43732.
- [49] T. Zacherle, P.C. Schmidt, M. Martin, Ab initio calculations on the defect structure of  $\beta$ -Ga<sub>2</sub>O<sub>3</sub>, *Phys. Rev. B* 87 (2013) 235206.
- [50] D.C. Koningsberger, R. Prins, *X-ray Absorption: Principles, Applications, Techniques of EXAFS, SEXAFS and XANES*, Wiley-Interscience, 1988.
- [51] J.B. Varley, J.R. Weber, A. Janotti, C.G. Van de Walle, Oxygen vacancies and donor impurities in  $\beta$ -Ga<sub>2</sub>O<sub>3</sub>, *Appl. Phys. Lett.* 97 (2010) 142106.
- [52] A. Bouzid, A. Pasquarello, Defect formation energies of interstitial C, Si, and Ge impurities in  $\beta$ -Ga<sub>2</sub>O<sub>3</sub>, *Phys. Status Solidi RRL* 13 (2019) 1800633.
- [53] C.J. Zeman, S.M. Kiehar, L.O. Jones, M.A. Mosquera, G.C. Schatz, Investigation of P-type doping in  $\beta$ - and  $\kappa$ -Ga<sub>2</sub>O<sub>3</sub>, *J. Alloys. Compd.* 877 (2021) 160227.
- [54] Y. Syryanyy, M. Zając, E. Guziejewicz, W. Wozniak, Y. Melikhov, M. Chernyshova, R. Ratajczak, I.N. Demchenko, Polarized dependence of soft X-ray absorption near edge structure of ZnO films implanted by Yb, *Mat. Sci. Semicon. Proc.* 144 (2022) 106609.
- [55] R. Storn, K. Price, Differential evolution - A simple and efficient heuristic for global optimization over continuous spaces, *Global Optim* 11 (1997) 341.
- [56] B. De Vries, *Lattice Site Location of Impurities in Group III Nitrides Using Emission Channeling* (Ph.D. Thesis), Leuven University, Leuven, Belgium, 2005.
- [57] T. Yoo, X. Xia, F. Ren, A. Jacobs, M.J. Tadjer, S. Pearton, H. Kim, Atomic-scale characterization of structural damage and recovery in Sn ion-implanted  $\beta$ -Ga<sub>2</sub>O<sub>3</sub>, *Appl. Phys. Lett.* 121 (2022) 072111.
- [58] A. Kovács, J. Sadowski, T. Kasama, M. Duchamp, R.E. Dunin-Borkowski, Effect of post-growth annealing on secondary phase formation in low-temperature-grown Mn-doped GaAs, *J. Phys. D: Appl. Phys.* 46 (2013) 145309.
- [59] A. Kovács, J. Sadowski, T. Kasama, J. Domagala, R. Mathieu, T. Dietl, R.E. Dunin-Borkowski, Voids and Mn-rich inclusions in a (Ga,Mn)As ferromagnetic semiconductor investigated by transmission electron microscopy, *J. Appl. Phys.* 109 (2011) 083546.
- [60] H.L. Huang, C. Chae, J.M. Johnson, A. Senckowski, S. Sharma, U. Singiseti, M. H. Wong, J. Hwang, Atomic scale defect formation and phase transformation in Si implanted  $\beta$ -Ga<sub>2</sub>O<sub>3</sub>, *APL Mater.* 11 (2023) 061113.
- [61] M. Peres, K. Lorenz, E. Alves, E. Nogales, B. Méndez, X. Biquard, B. Daudin, E. G. Villora, K. Shimamura, Doping  $\beta$ -Ga<sub>2</sub>O<sub>3</sub> with europium: influence of the implantation and annealing temperature, *J. Phys. D: Appl. Phys.* 50 (2017) 325101.
- [62] E. Wendler, O. Bilani, K. Gärtner, W. Wesch, M. Hayes, F.D. Auret, K. Lorenz, E. Alves, Radiation damage in ZnO ion implanted at 15 K, *Nucl. Instrum. Methods Phys. Res. B* 267 (2009) 2708.
- [63] M.L. Swanson, The study of lattice defects by channeling, *Rep. Prog. Phys.* 45 (1982) 47.
- [64] J. Eymer, N. Soubie, L. Capello, F. Rieutord, X-ray scattering study of hydrogen implantation in silicon, *J. Appl. Phys.* 99 (2006) 103509.
- [65] M. Wójcik, J. Gaca, P. Caban, A. Turoś, HRXRD study of ZnO single crystals bombarded with Ar ions, *Materiały Elektroniczne (Electronic Materials)* 44 (3) (2016) 9.